JAAS

PAPER

Occurrence of gas flow rotational motion inside the ICP torch: a computational and experimental study

Cite this: *J. Anal. At. Spectrom.*, 2014, **29**, 249

Maryam Aghaei,*[a] Luca Flamigni,[b] Helmut Lindner,[a] Detlef Günther[b] and Annemie Bogaerts[a]

Received 18th September 2013
Accepted 14th November 2013

DOI: 10.1039/c3ja50302j

www.rsc.org/jaas

An inductively coupled plasma, connected to the sampling cone of a mass spectrometer, is computationally investigated. The occurrence of rotational motion of the auxiliary and carrier gas flows is studied. The effects of operating parameters, *i.e.*, applied power and gas flow rates, as well as geometrical parameters, *i.e.*, sampler orifice diameter and injector inlet diameter, are investigated. Our calculations predict that at higher applied power the auxiliary and carrier gas flows inside the torch move more forward to the sampling cone, which is validated experimentally for the auxiliary gas flow, by means of an Elan 6000 ICP-MS. Furthermore, an increase of the gas flow rates can also modify the occurrence of rotational motion. This is especially true for the carrier gas flow rate, which has a more pronounced effect to reduce the backward motion than the flow rates of the auxiliary and cooling gas. Moreover, a larger sampler orifice (*e.g.*, 2 mm instead of 1 mm) reduces the backward flow of the auxiliary gas path lines. Finally, according to our model, an injector inlet of 2 mm diameter causes more rotations in the carrier gas flow than an injector inlet diameter of 1.5 mm, which can be avoided again by changing the operating parameters.

1. Introduction

The inductively coupled plasma (ICP) is an efficient atomization, ionization and excitation source, widely used for inorganic elemental and isotopic analysis by means of mass spectrometry (ICPMS) or optical emission spectrometry (ICP-OES). Therefore optimization of its analytical performance is crucial. A number of studies have been performed for the effect of the presence of a mass spectrometer interface on ICPMS,[1–8] as well as for the effect of the ICP geometrical parameters (*i.e.*, position and diameter of the sampler orifice, as well as gas inlet diameter) on the plasma characteristics.[9–16] These observations all suggest that the use of an interface with different orifice sizes significantly affects the plasma characteristics.

Besides the optimization of the geometrical parameters, also the effect of the operating parameters, such as the applied rf power, the carrier gas and auxiliary gas flow rates, the pressure downstream the sampler and the sample composition, has also been of tremendous interest.[15–27]

In recent years, we investigated the effect of operating conditions (rf power and gas flow rates) and geometrical parameters (*i.e.*, position and size of sampler orifice, as well as injector inlet diameter) on the typical plasma characteristics, such as the plasma temperature, pressure, electron density and plasma velocity.[8,28,29] However, the operating and geometrical parameters can also influence the flow path lines inside the torch. Indeed, it is difficult to measure the gas flow characteristics along the entire ICP torch and researchers are mostly interested in the coil and after the coil region in the case of ICP-OES, and in the sampler cone region in the case of ICPMS. Nevertheless, the change in flow path lines and the occurrence of rotational motions in the torch have been investigated experimentally by a few research groups.[2,30] Noise-power spectra of emission signals from an ICP discharge are shown in ref. 30. It is indicated by Horlick *et al.* that in the 0–500 Hz region a peak in the noise power spectrum occurs which appears to be the result of rotation of the plasma discharge at a frequency ranging from 200 to 400 Hz. The exact position and intensity of these peaks were dependent on the exact experimental conditions, *e.g.* rf power, coolant gas flow rate and torch design. This was explained by rotation of the slightly asymmetric plasma and that the asymmetry was primarily induced by air entrainment, which can be reduced by using a so-called "tall torch".[30] Moreover, the presence of rotations has been confirmed by high-speed photography of plasma fluctuations in ref. 2. Houk *et al.* indicated that the rotations can be observed in horizontal plasmas as well as vertical plasmas. However, the insertion of a sampling cone blocks the downstream region where the rotations are prominent. Therefore, the rotations observed from yttrium oxide emission were found to be less evident in the presence of a sampler. It should be mentioned that the observed

[a]*Research group PLASMANT, Department of Chemistry, University of Antwerp, Universiteitsplein 1, B-2610 Wilrijk-Antwerp, Belgium. E-mail: Maryam.aghaei@uantwerpen.be*

[b]*Swiss Federal Institute of Technology, Laboratory of Inorganic Chemistry, ETH Zürich, Wolfgang-Pauli-Strasse 10, CH-8093 Zürich, Switzerland*

rotational motions reported from both groups occurred downstream the load coils (*i.e.*, close to the sampling cone), while in this manuscript the rotations occurring upstream the load coils inside the ICP torch will be investigated. Moreover, the backward motion of the gas flow could also be seen (although it was not discussed) in ref. 15, which presents a numerical simulation of an ICP torch at atmospheric pressure.

Although it is not specifically mentioned in ICP related papers, the backward gas flow motion inside the torch can be explained by fluid dynamics concepts. Indeed, when two layers of fluid in contact with each other move at different speeds, there will be a shear force depending on the flow viscosity between them.[31,32] As we can consider the flow as laminar, this force can be assumed to act between all laminar layers of the flow entering from three different inlets with different flow rates.

It has already been demonstrated in our previous studies[16,29] that the auxiliary gas flow and even the carrier gas flow do not always move in the forward direction inside the torch. This can be explained by the difference in velocities between the carrier gas, auxiliary gas and cooling gas flows. According to the different initial flow rates, each flow moves with a different velocity. Note that each inlet has a specific area and especially the auxiliary gas inlet is much wider than the carrier and cooling gas inlets. This means that the auxiliary gas can enter more freely than the carrier and cooling gases. As can be seen in Fig. 1, the carrier gas flow accelerates faster than the auxiliary gas flow. Therefore, a shear force takes place between the faster carrier gas flow and the slower auxiliary gas flow: $F = \eta A \frac{\partial V_x}{\partial r}$. Here η is the dynamic fluid viscosity, A is the area of contact, V_x is the axial velocity and r is the radial distance. A similar force exists between the faster cooling gas flow and the slower auxiliary gas flow. However, it should be noted that the auxiliary gas flow comes into contact earlier with the carrier gas flow than with the cooling gas flow because of a difference in the length of the inlets. Therefore, the auxiliary gas flow is first affected by a shear force from the carrier gas flow before it comes into contact with the cooling gas flow. When the cooling gas reaches the end of the auxiliary inlet, it also applies a shear force on the auxiliary gas flow and the overall result will be a backward turn and again a forward motion of the auxiliary gas flow. Similar behavior is sometimes observed for the carrier gas flow (see below).

In the present study we aim at obtaining a better insight into the occurrence of the backward gas flows in the torch and we hope to find parameters or operating conditions to control these motions. Especially for the carrier gas flow, which carries the sample, any deviation from the central axis leads to a longer transit time and loss of intensity and should be avoided. Note that this is especially important after the particle evaporation has taken place.[33] Also, it brings the sample particles to the outer region of the torch, thereby lowering the chance that the sample exits through the sampler. Hence, the detection efficiency becomes lower as some part of the sample is lost in the torch and not effectively sampled through the plasma–vacuum interface. It is therefore of crucial importance to know which parameters and to what extent they affect the rotational gas flows inside the torch, as this knowledge will allow us to optimize the conditions needed to avoid rotational gas flows inside the ICP torch. Note that in this paper we only focus on the rotational motion and not on ionization of the analyte. However, the ionization efficiency is also affected by the plasma conditions and this has a large influence on the analytical performance of ICPMS as well, but this is beyond the scope of the present paper.

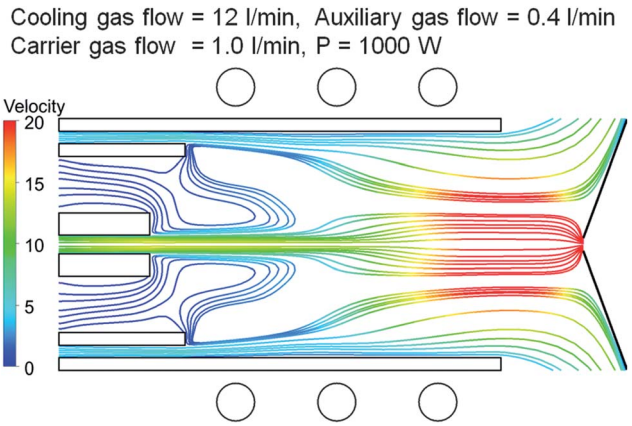

Fig. 1 2D gas flow velocity path lines originating from the carrier gas, auxiliary gas and cooling gas inlets, colored by velocity in m s^{-1}. The applied power is 1000 W. The carrier gas, auxiliary gas and cooling gas flow rates are 1.0, 0.4 and 12 L min^{-1}, respectively. The injector inlet diameter and sampler orifice diameter are 1.5 mm and 1.0 mm, respectively.

2. Description of the model

To calculate the gas flow inside the entire torch, a 2D axisymmetric geometry is set up and inserted in a commercial computational fluid dynamics (CFD) program, called Fluent v13.0.0 (ANSYS).[34,8] The gas entering from the three concentric tubes of the ICP torch flows inside the active plasma zone of the torch, and finally through the sampler cone or towards the open sides of the torch, which are filled with ambient gas, taken to be argon for simplicity. The ICP gas stream is also assumed to be pure argon. The temperature and velocity are calculated by solving coupled differential equations, such as the Navier–Stokes equations and the energy conservation equation, where certain terms are added, *e.g.*, power coupling as a source term and the emitted radiation as an energy loss term. The calculations are performed by a finite-volume method taking into account the whole calculation region and its boundary conditions. The equations are solved iteratively until a stable solution is obtained. The electric fields are calculated as user defined scalars (UDSs) in Fluent. For defining the heat capacity and thermal conductivity, a number of self-written modules were added as user-defined functions (UDFs), as described in ref. 35. The plasma species considered in the model are Ar atoms, singly charged and doubly charged Ar ions, and electrons. As is fully described in ref. 35, their transport properties are calculated by kinetic theory. By comparing the calculation results with the experiments in ref. 16, it was verified that applying the

Table 1 Operating conditions and boundary conditions in the model

Frequency	27 MHz
Input power	1000–1500 W
Carrier gas flow rate	Ar; 1.0–2.5 L min^{-1}
Auxiliary gas flow rate	Ar; 0.4–2.0 L min^{-1}
Cooling gas flow rate	Ar; 12–18 L min^{-1}
Ambient pressure	101 325 Pa
Exhaust pressure	101 225 Pa
Pressure downstream the sampler cone	1.32×10^{-3} atm (1 torr)
Injector inlet inner diameter	1.5 mm, (2 mm)
Injector inlet wall thickness	1.75 mm, (1.5 mm)
Distance between the inner diameter of the injector inlet and the cooling inlet	8.25 mm, (8 mm)
Cooling and auxiliary inlet wall thickness	1 mm
Inlet gas temperature	297 K
Sampler cone temperature	500 K
Sampler orifice diameter	1 and 2 mm
Sampler distance from the load coil	10 mm

local thermodynamic equilibrium (LTE) condition to the plasma is a reasonable approximation.

The boundary conditions used in the model, as well as the operating parameters for which calculations will be performed here, are displayed in Table 1. In the current study, the position of the sampler is kept fixed at 10 mm distance from the load coil. The sampler orifice diameter is also kept fixed at 1 mm, except when mentioned otherwise. Furthermore, the power is kept constant at 1000 W, unless specified otherwise, and the frequency of the harmonic external electric current density is 27 MHz. The downstream pressure of the sampler is fixed at 1 torr, similar to experimental setups.[3,17] The ambient gas pressure and exhaust pressure are set to 1 atm and 0.99 atm, respectively. The model was validated by the experiments reported in ref. 8, 16, 28 and 29.

3. Results and discussion

When the auxiliary gas enters the torch, it typically does not go directly to the coil area. Indeed, in all the path line profiles we calculated until now,[8,28,29] similar behavior could be seen, characterized by a forward, then backward and again a forward movement of the auxiliary gas. Experimental observations also suggest that the same rotational flow pattern inside the torch might occur (see below). However, by changing some operating parameters, which will be presented in Section 3.1, we found that it is possible to reduce or even remove these backward curves and to obtain a condition where the auxiliary gas only moves forward along the torch. It should, however, be noted that if the auxiliary gas goes very straight along the torch and does not pass through the area where the maximum power coupling occurs (see violet contours in Fig. 2), the efficiency of heating in the ICP decreases substantially. This means that we should find the optimum condition at which no backward motions occur and at the same time the auxiliary gas still follows a curved path along the torch, still passing through the efficient power coupling area. In other words, "forward curved" path lines along the torch are favorable. In Section 3.1, we try to reach this optimum condition.

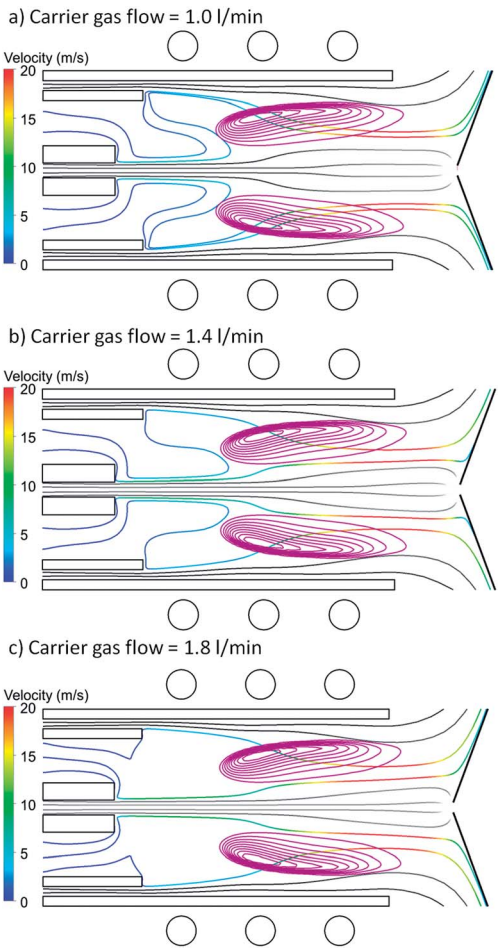

Fig. 2 Effect of carrier gas flow rate: 2D gas flow velocity path lines originating from the auxiliary gas inlet, colored by velocity in m s^{-1}, as well as from the carrier gas and cooling gas inlets, colored in black. The carrier gas flow rate is taken as 1 (a), 1.4 (b) and 1.8 (c) L min^{-1}, whereas the cooling and auxiliary gas flow rates are kept fixed at 12 and 0.4 L min^{-1}, respectively. The injector inlet diameter and the sampler orifice diameter are 1.5 mm and 1.0 mm, respectively. The violet contours demonstrate the area of external power coupling.

Besides the auxiliary gas flow, the carrier gas flow path lines might also exhibit some backward curved motion, depending on the injector inlet diameter, which affects the previous speed up of the carrier gas flow compared to the other gas flows. This is even more crucial for the analytical performance of the ICP, as the sample particles are introduced from the injector inlet, and they should be able to reach the sampler orifice, after atomization. Therefore, Section 3.2 will be devoted to how the rotational motion of the carrier gas flow can be removed.

3.1. Rotational behavior in the auxiliary gas flow

In this section, the effect of the different flow rates, power and sampler orifice diameter on the rotational motion of the auxiliary gas flow will be investigated. The injector inlet diameter is kept fixed at 1.5 mm.

a.Effect of carrier gas flow rate. Fig. 2 presents the 2D velocity path lines for fixed values of cooling gas and auxiliary gas flow rates, *i.e.*, 12 and 0.4 L min^{-1}, respectively, while varying the carrier gas flow rate as 1.0 (a), 1.4 (b) and 1.8 (c) L min^{-1}. Note that the conditions of Fig. 2(a) are the same as for Fig. 1, but a lower number of path flow lines is depicted for the sake of clarity. Furthermore, only the auxiliary gas is shown with colored lines, and also the area of external power coupling is indicated. It can be seen from Fig. 2(a) that a strong rotational motion occurs in the auxiliary gas flow when the carrier gas flow rate is 1.0 L min^{-1} (see the colored lines). When increasing the carrier gas flow rate to 1.4 L min^{-1} (Fig. 2(b)), a part of the auxiliary gas still shows backward flow but another part goes forward in the torch and does not turn backward. When further increasing the carrier gas flow rate to 1.8 L min^{-1}, no rotational motion occurs in the torch (see Fig. 2(c)), *i.e.*, the auxiliary gas only flows in the forward direction while it still passes through the area of maximum power coupling (violet contours). Hence, by applying high enough carrier gas flow rates (*i.e.*, 1.8 L min^{-1} when the auxiliary and cooling gas flow rates are 0.4 and 12 L min^{-1}) we can prevent the formation of rotational flow inside the torch. Indeed, when comparing Fig. 2(a–c), it is clear that by increasing the flow rate of the carrier gas, which is accelerated toward the sampler due to the high pressure drop behind the sampler cone, the expansion of the carrier gas flow is less pronounced and also starts further along the torch. This allows more auxiliary gas flow to reach the center and therefore the auxiliary gas flow can go more in the forward direction.

b.Effect of auxiliary gas flow rate. Fig. 3 illustrates the flow path lines for a fixed cooling gas flow rate of 12 L min^{-1}, but varying the auxiliary gas flow rate and at the same time the carrier gas flow rate, to avoid rotational motion in the auxiliary gas. Our calculations predict that for the same cooling gas flow rate (12 L min^{-1}), there exists for each auxiliary gas flow rate a transition point for the carrier gas flow rate to avoid rotational motion in the auxiliary gas. This transition point rises with the value of the auxiliary gas flow rate. Indeed, at 0.4 L min^{-1} auxiliary gas flow rate, this transition point was observed at 1.8 L min^{-1} carrier gas flow rate (*cf.* Fig. 2 above), whereas it was found to be 2.0 L min^{-1} and 2.2 L min^{-1} for auxiliary gas flow rates of 0.6 and 0.8 L min^{-1}, respectively (see Fig. 3). It should

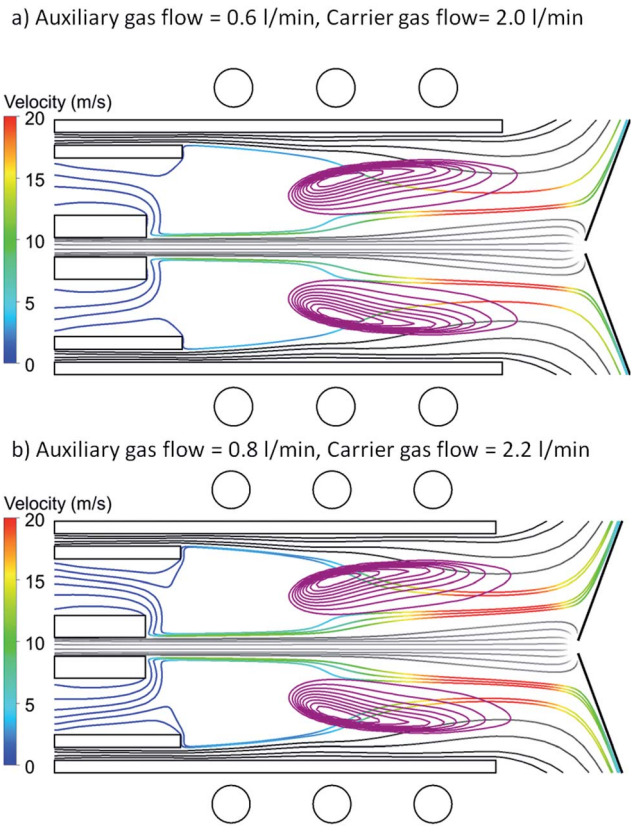

Fig. 3 Effect of auxiliary and carrier gas flow rates: 2D gas flow velocity path lines originating from the auxiliary gas inlet, colored by velocity in m s^{-1}, as well as from the carrier gas and cooling gas inlets, colored in black. The auxiliary and carrier gas flow rates are taken as 0.6, 2.0 (a) and 0.8, 2.2 (b) L min^{-1}, respectively, whereas the cooling gas flow rate is kept fixed at 12 L min^{-1}. The injector inlet diameter and the sampler orifice diameter are 1.5 mm and 1.0 mm, respectively. The violet contours demonstrate the area of external power coupling.

be mentioned that an increase of the carrier gas flow rate to higher values, while keeping the injector inlet diameter fixed, causes the Reynolds number to exceed the critical value of 2300, which is considered to be the upper limit for assuming the flow as laminar in a pipe flow. Indeed, the Reynolds numbers for the conditions presented in Fig. 3(a) and (b) are 1900 and 2100, respectively. We performed the same calculation with an auxiliary gas flow rate of 1.0 L min^{-1} in which the transient flow rate for the carrier gas was 2.5 L min^{-1}. We did not show this result in Fig. 3 as the Reynolds number exceeds the critical value and the results are less precise as the assumption of the laminar regime is not valid anymore, although it should be mentioned that up to a Reynolds number of 4000, the flow is still in the transient regime and not in the turbulent regime.

c.Effect of cooling gas flow rate. For practical use of ICPMS, commercial instruments sometimes do not allow to vary the carrier gas and auxiliary gas flow rates in a wide range. If for instance 1.4 L min^{-1} and 0.4 L min^{-1} are acceptable and favorable values for the carrier gas and auxiliary gas flow rates, this gives rise to rotational motion in the auxiliary gas, when the cooling gas flow rate is 12 L min^{-1}, as is illustrated in Fig. 2(b) above. However, when increasing the cooling gas flow rate to 14

and 16 L min^{-1}, keeping the carrier gas and auxiliary gas flow rates fixed, the rotational motion in the auxiliary gas flow can also be reduced and even avoided, as can be seen from Fig. 4. In Fig. 4(a), some rotational flow is still observed, but when the cooling gas flow rate is 16 L min^{-1}, as illustrated in Fig. 4(b), the backward motion is avoided. Therefore, if experimentally we cannot increase the carrier gas and auxiliary gas flow rates, we can still control the occurrence of rotational motion of the auxiliary gas by varying the cooling gas flow rate. However, this gives rise to higher gas consumption. Furthermore, it is clear that the effect of the cooling gas flow rate is minor compared to the effect of the carrier gas flow rate. Indeed, the carrier gas is much faster inside the torch due to the entrainment forces acting upon it, while the cooling gas exits more slowly from the open sides of the torch. Therefore, only 0.8 L min^{-1} increase in the carrier gas flow rate (*cf.* Fig. 2(a) and (c)) can change the behavior of the auxiliary gas, while the cooling gas should increase by 4 L min^{-1} to have the same effect.

d.Effect of applied power. Besides the gas flow rates, we found that the external power also has an effect on the rotational behavior of the auxiliary gas. Fig. 5 shows the 2D velocity path lines with 12 L min^{-1} cooling gas, 0.4 L min^{-1} auxiliary gas and 1.0 L min^{-1} carrier gas flow rates, at 750 W (a), 1000 W (b), 1250 W (c), and 1500 W (d) external power. Note that Fig. 5(b) corresponds to the condition of Fig. 2(a). The effect of power on the fundamental plasma characteristics is discussed in detail in ref. 28. Here we only focus on the presence of backward motion inside the torch. The external power seems to have a significant effect on the auxiliary gas flow pattern. In Fig. 5(a) (750 W), the auxiliary gas goes in the forward direction over a longer distance, before it turns backward, while in Fig. 5(b) (1000 W) and Fig. 5(c) (1250 W), this "turn" occurs earlier, and finally at 1500 W (Fig. 5(d)) and no backward flow is observed. Although the effect of external power is shown here to control the auxiliary gas movement inside the ICP torch, we do not recommend this condition of high power. Indeed, it is shown in Fig. 5(d) that the auxiliary gas, which is supposed to heat up the carrier gas, does not pass through the area of efficient power coupling, whereas the cooling gas, which is meant for supporting the plasma and for cooling, now mostly receives the external energy and is heated up, which should be avoided due to a higher risk of melting the torch and because of reducing the cooling efficiency. A more thorough discussion about applying 1500 W external power is provided in ref. 28.

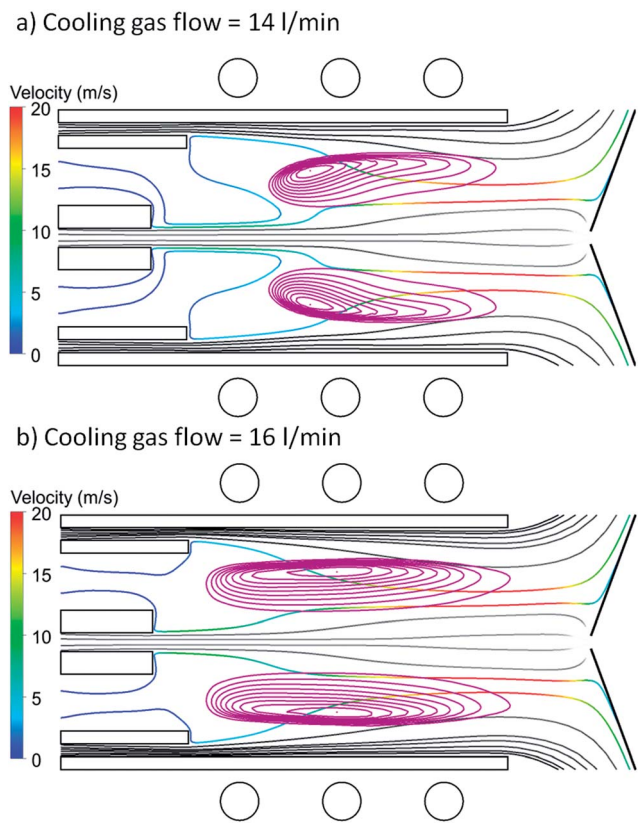

Fig. 4 Effect of cooling gas flow rate: 2D gas flow velocity path lines originating from the auxiliary gas inlet, colored by velocity in m s^{-1}, as well as from the carrier gas and cooling gas inlets, colored in black. The cooling gas flow rate is taken as 14 (a) and 16 (b) L min^{-1}, whereas the carrier gas and auxiliary gas flow rates are kept fixed at 1.4 and 0.4 L min^{-1}, respectively. The injector inlet diameter and the sampler orifice diameter are 1.5 mm and 1.0 mm, respectively. The violet contours demonstrate the area of external power coupling.

To validate our model predictions, we compared them with experimental data. For this purpose, an Elan 6000 ICP-MS (Perkin Elmer, Waltham, MA, USA) was used, and sodium chloride aerosols generated by laser ablation (LSX 500, Cetac Technologies, Omaha, NB, USA) were introduced to the ICP torch from the auxiliary gas inlet instead of the injector inlet. Fig. 6 shows 2D images of the ICP torch with an applied power of 800 W (first row) and 1400 W (second row). The carrier (injector) gas only contains Ar, with a flow rate of 0.5 L min^{-1} (first column), 1.0 L min^{-1} (second column) and 1.5 L min^{-1} (third column) through an opening of 2 mm diameter. The auxiliary gas and cooling gas flow rates are kept fixed at 1.3 and 16 L min^{-1}, respectively. The sodium atomic emission line at 589 nm (shown in yellow) is captured using an ICCD camera[36] through an optical interference filter. Image processing is performed using Fiji[37] and ImageJ[38] which are software tools for microscopy. For each pixel composing the image, the maximum value is searched among 50 pictures of 5 ms exposure each, providing this way information about all images at once. The plasma emission background is subtracted before evaluation. In this way, only the emission produced by the laser aerosol particles and introduced from the auxiliary gas inlet is visible. In blue, the torch configuration before the experiment, *i.e.*, without plasma and without interference filter, is shown.

Fig. 6 illustrates a non-homogeneous distribution of the intensity (yellow) in the first row (800 W), between the first and the second winding of the coil, which hints at whirls in this region. By increasing the applied power we can observe an improvement, *i.e.*, less pronounced rotational motion. Indeed, in the second row (1400 W), the region between the first and the second winding of the coil is much smoother and there is no real evidence for a curved gas flow pattern. It is important to mention that experimentally we cannot be very sure about the exact values of the power that are actually applied, so Fig. 6 can

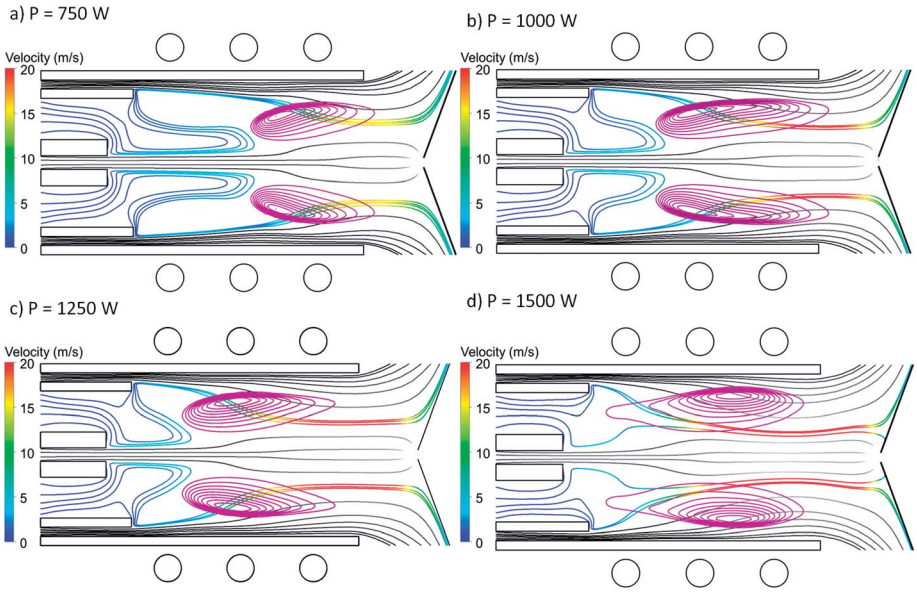

Fig. 5 Effect of power: 2D gas flow velocity path lines originating from the auxiliary gas inlet, colored by velocity in m s^{-1}, as well as from the carrier gas and cooling gas inlets, colored in black. The applied power is taken as 750 (a), 1000 (b), 1250 (c) and 1500 (d) W. The carrier gas, auxiliary gas and cooling gas flow rates are 1.0, 0.4 and 12 L min^{-1}, respectively. The injector inlet diameter and sampler orifice diameter are 1.5 mm and 1.0 mm, respectively. The violet contours demonstrate the area of external power coupling.

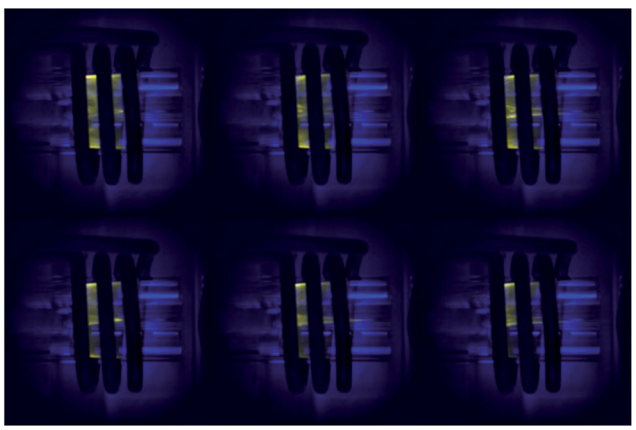

Fig. 6 False-color images of background-corrected emission produced by sodium atom clouds (yellow) captured at low time resolution, overlaid on the image of the torch without plasma (blue). From left to right, the settings for the carrier gas flow rate are: 0.5, 1, 1.5 L min^{-1} Ar. The first row was measured while applying 800 W and the second row 1400 W rf power.

only reveal the qualitative effect of (low and high) power. Furthermore, the gas flow rates in the torch are also subject to uncertainties, since the mass flow controllers are not 100% accurate and the cooling gas flow rate cannot be controlled through the Elan 6000 ICP-MS software. For these reasons, we are not able to compare all the calculated conditions one-to-one with the experiments, but we rather discuss common trends. As mentioned above, each column in Fig. 6 represents a different carrier gas flow rate, but in all three cases, the rotational flow behavior can be deduced from the intensity distribution. Indeed, it was mentioned in Section (b) above that for each auxiliary gas flow rate there is a transition value of the carrier gas flow rate beyond which no rotation occurs anymore. As the auxiliary gas flow rate in this setup is fixed to 1.3 L min^{-1}, we expect this transition point to occur at much higher carrier gas flow rates than the system allows, *i.e.*, at least 2.5 L min^{-1} (*cf.* Fig. 3(c) above). This explains why we observe the rotations for all carrier gas flow rates used (*i.e.*, 0.5, 1.0 and 1.5 L min^{-1}), as they are below 2.5 L min^{-1}. This is, at least, in qualitative agreement with our model predictions.

Fig. 7 provides evidence that we are actually tracking particle clouds, which are distinctly visible at short integration times (compared to the particle travel time inside the plasma, which is in the order of a few milliseconds), but they will appear as soft lines at longer integration times due to motion and diffusion (Fig. 6). The applied power in this case is 800 W and the carrier gas flow rate is again 0.5 (left), 1.0 (middle) and 1.5 (right) L min^{-1}. The other measurement conditions are exactly the same as for Fig. 6, except that 50 μs exposure time was used instead of

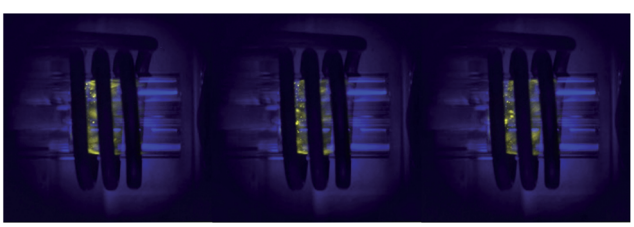

Fig. 7 False-color images of background-corrected emission produced by sodium atom clouds (yellow) captured at high time resolution, overlaid on the image of the torch without plasma (blue). From left to right, the settings for the carrier gas flow rate are: 0.5, 1, 1.5 L min^{-1} Ar. The applied rf power was 800 W.

5 ms, so that no plasma emission background subtraction was necessary. The emission pattern in Fig. 7 is indeed the same as in the upper row of Fig. 6, but at long integration times (5 ms) the flight patterns are more visible due to the absence of strong localized emission clouds and due to the superposition of many movement tracks. In summary, it can be deduced from Fig. 6 and 7 that (i) some rotational motion may indeed occur in the auxiliary gas flow and (ii) this rotational motion can be reduced, or even avoided, by increasing the applied rf power.

e.Effect of sampler orifice diameter. Besides the operating parameters, *i.e.*, gas flow rates and applied power, our calculations predict that a change in the geometrical parameters can also affect the rotational behavior inside the ICP torch. Fig. 8 presents 2D velocity path lines for fixed values of cooling gas, auxiliary gas and carrier gas flow rates, *i.e.*, 12, 0.4 and 1.0 L min^{-1}, respectively, at an applied power of 1000 watt, with sampler orifice diameters of 1 mm (a) and 2 mm (b). Note that Fig. 8(a) corresponds to Fig. 2(a). It appears that the occurrence of strong rotational flow (as in Fig. 8(a)) becomes less pronounced when the sampler cone has a larger orifice (Fig. 8(b)). This can be explained because with a larger sampler orifice, the auxiliary gas flow has the chance to enter the mass spectrometer, accompanying the carrier gas flow, as was demonstrated in ref. 29. Consequently, the auxiliary gas flow is "sucked" toward the sampler orifice, thereby reducing the backward motion.

3.2. Rotational behavior in the carrier gas flow

In this section, the effect of injector inlet diameter, as well as of the different flow rates, on the rotational motion of the carrier gas flow pattern will be investigated. For this purpose, the injector inlet diameter is increased from 1.5 mm to 2 mm, whereas the sampler orifice diameter is kept fixed at 1 mm.

Since the sample particles (or aerosols) are introduced from the injector inlet, optimizing the carrier gas flow path lines is crucial to guarantee that the introduced sample can reach the sampler orifice. As mentioned above, this implies that the ion cloud of the sample is led forward in the torch and along the central channel. Otherwise, when the ion cloud spreads out from the central channel due to diffusion, it may be possible to lose part of the sample, as it may follow the path lines which exit from the open sides of the torch instead of through the sampler orifice.

a.Effect of injector inlet diameter. In Section 3.1 the injector inlet diameter was kept fixed at 1.5 mm, and in this case, the

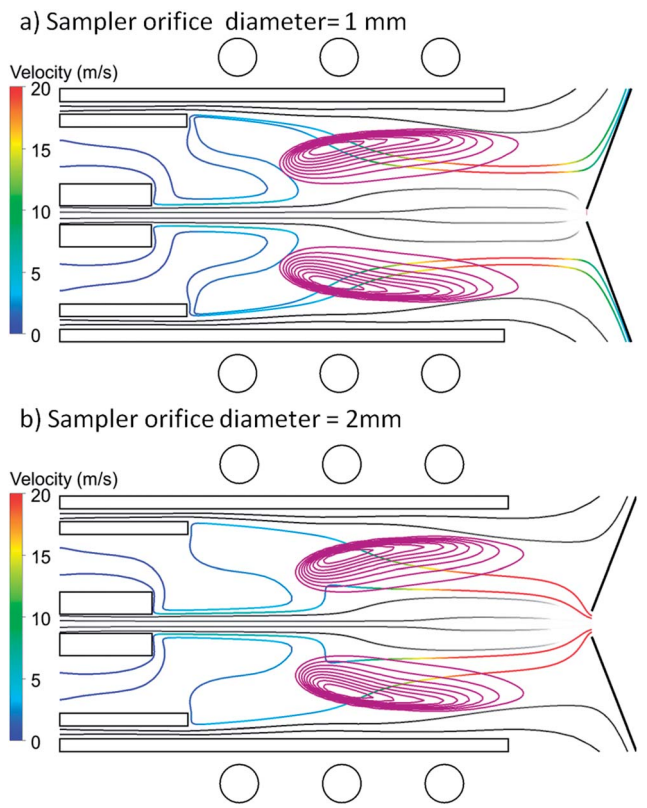

Fig. 8 Effect of sampler orifice diameter: 2D gas flow velocity path lines originating from the auxiliary gas inlet, colored by velocity in m s^{-1}, as well as from the carrier gas and cooling gas inlets, colored in black. The sampler orifice diameter is taken as 1 (a) and 2 (b) mm. The carrier gas, auxiliary gas and cooling gas flow rates are 1.0, 0.4 and 12 L min^{-1}, respectively. The injector inlet diameter is 1.5 mm. The violet contours demonstrate the area of external power coupling.

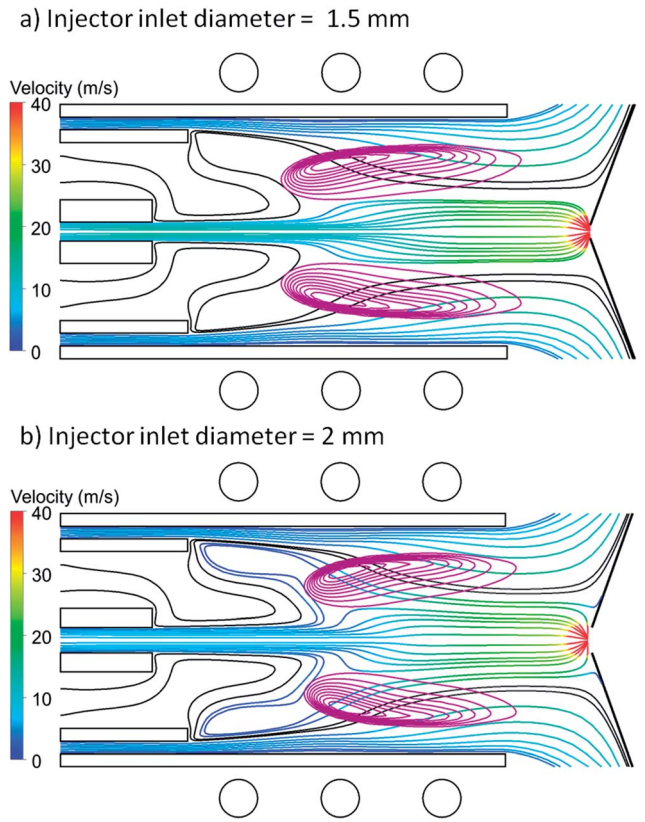

Fig. 9 Effect of injector inlet diameter: 2D gas flow velocity path lines originating from the carrier gas and cooling gas inlets, colored by velocity in m s^{-1}, and from the auxiliary gas inlet, colored in black. The injector inlet diameter is taken as 1.5 (a) and 2.0 (b) mm, and the sampler orifice diameter is 1.0 mm. The carrier gas, auxiliary gas and cooling gas flow rates are 1.0, 0.4 and 12 L min^{-1}, respectively. The violet contours demonstrate the area of external power coupling.

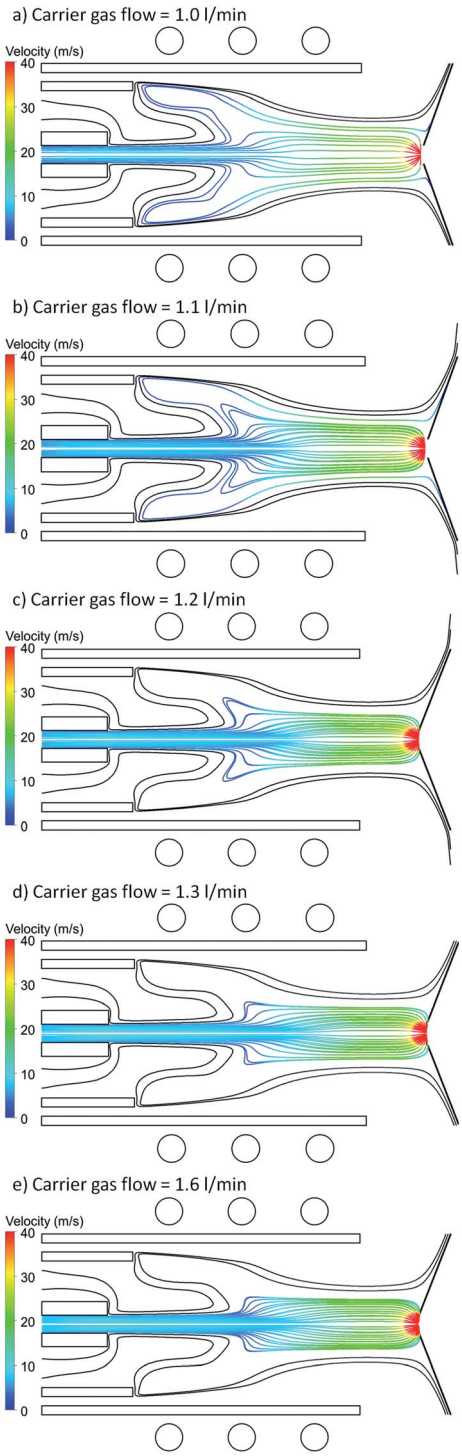

Fig. 10 Effect of carrier gas flow rate: 2D gas flow velocity path lines originating from the carrier gas inlet, colored by velocity in m s^{-1}, and from the auxiliary gas inlet, colored in black. The cooling gas path lines are omitted for the sake of clarity. The carrier gas flow rate is taken as 1 (a), 1.1 (b), 1.2 (c), 1.3 (d) and 1.6 (e) L min^{-1}. The cooling gas and auxiliary gas flow rates are 12 and 0.4 L min^{-1}, respectively. The injector inlet diameter and sampler orifice diameter are 2.0 mm and 1.0 mm, respectively.

carrier gas never exhibits rotational behavior, at least for the wide range of conditions investigated by our model. However, when increasing the injector inlet diameter to 2 mm, a drastic change in the carrier gas path flow lines can be observed. Fig. 9 shows 2D velocity path lines for the same operating parameters, *i.e.*, 12, 0.4 and 1.0 L min^{-1} for the cooling gas, auxiliary gas and carrier gas flow rates, respectively, and an applied power of 1000 W, with the injector diameter of 1.5 mm (a) and 2 mm (b). Again Fig. 9(a) corresponds to Fig. 2(a), but now the colored lines represent the carrier gas and cooling gas flows, whereas the black lines show the auxiliary gas path lines. By comparing the velocity difference of the carrier gas and cooling gas flows in Fig. 9(a) and (b), it can be seen that by enlarging the injector inlet diameter to 2 mm, the carrier gas flow is no longer much faster than the cooling gas. As a result, the shear force from the cooling gas flow, which affects the auxiliary gas, could now also partly affect the carrier gas flow. Hence, a larger injector inlet diameter causes a change in the carrier gas flow path lines, and a backward motion of the carrier gas flow becomes apparent for an injector diameter of 2 mm. This is not favorable because if the introduced sample particles follow the backward lines, they may be lost in the torch and they cannot be effectively transferred to the mass spectrometer. Fig. 9(b) indeed shows that not all carrier gas path lines are directed to the sampler orifice. Nevertheless, an injector inlet diameter of 2 mm is quite common in ICP setups.[39] Therefore, in order to avoid this rotational flow in the carrier gas path lines, several calculations are performed with different operational parameters, as will be discussed in the following sections.

It should be mentioned that Lindner *et al.*[16] discussed that for every injector inlet diameter, there is a transition flow rate for the carrier gas to achieve a central channel in the ICP torch. For example, for the injector inlet diameter of 2 mm, the carrier gas flow rate should exceed 0.4 L min^{-1} to make a central channel. In the current study, we meet that condition and hence there is a central channel at all conditions investigated, but still not all of the carrier gas flow goes forward to the sampler orifice. Hence, in the present paper, after meeting the minimum criterion for obtaining a central channel, as discussed in ref. 16, we define an additional minimum gas flow rate (*i.e.*, higher than the minimum flow rate in ref. 16) to optimize the sample transfer by avoiding any backward motion in the carrier flow.

b.Effect of carrier gas flow rate. Fig. 10 presents 2D velocity path lines for fixed values of cooling gas and auxiliary gas flow rates, *i.e.*, 12 and 0.4 L min^{-1}, respectively, while varying the carrier gas flow rate as 1.0 (a), 1.1 (b), 1.2 (c), 1.3 (d), and 1.6 (e) L min^{-1}. The carrier gas flow is represented by colored lines, whereas the auxiliary gas is shown with black lines. The cooling gas flow path lines are omitted here, for the sake of clarity. As mentioned above, the injector inlet diameter and sampler orifice diameter are kept fixed at 2 mm and 1 mm, respectively. It is clear from Fig. 10 that a higher carrier gas flow rate results in a gradual drop in the backward flows of the carrier gas. The effect is most pronounced when the carrier gas flow rate increases from 1.1 to 1.2 L min^{-1} (*cf.* Fig. 10(b) and (c)). When reaching 1.3 and especially 1.6 L min^{-1} carrier gas flow rate, the rotational motion has completely disappeared (see Fig. 10(d) and (e)).

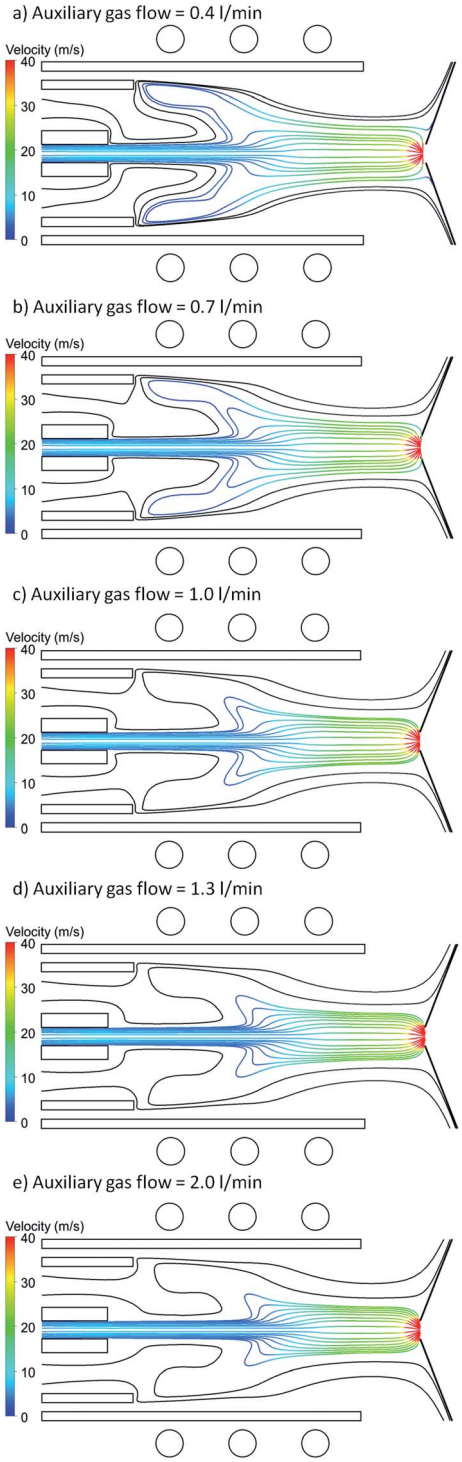

Fig. 11 Effect of auxiliary gas flow rate: 2D gas flow velocity path lines originating from the carrier gas inlet, colored by velocity in m s^{-1}, and from the auxiliary gas inlet, colored in black. The cooling gas path lines are omitted for the sake of clarity. The auxiliary gas flow rate is taken as 0.4 (a), 0.7 (b), 1.0 (c), 1.3 (d) and 2.0 (e) L min^{-1}. The cooling gas and carrier gas flow rates are 12 and 1.0 L min^{-1}, respectively. The injector inlet diameter and sampler orifice diameter are 2.0 mm and 1.0 mm, respectively.

c.Effect of auxiliary gas flow rate. Fig. 11 illustrates the flow path lines for fixed cooling gas and carrier gas flow rates of 12 and 1.0 L min^{-1}, respectively, but varying the auxiliary gas flow rate from 0.4 (a) to 0.7 (b), 1.0 (c), 1.3 (d) and 2.0 (e) L min^{-1}. Note that Fig. 11(a) corresponds to Fig. 10(a), but is repeated here for the sake of clarity. It is clear that by increasing the auxiliary gas flow rate from 0.4 to 0.7 L min^{-1}, the fraction of carrier gas path lines which move backward has dropped (*cf.* Fig. 11(a) and (b)). For an auxiliary gas flow rate of 1.0 L min^{-1} (see Fig. 11(c)), the large backward rotational motion has disappeared and only some deviation from the forward motion is observed. Our calculations predict that this deviation cannot be completely removed by increasing the auxiliary gas flow rate to 1.3 L min^{-1} (see Fig. 11(d)). We performed calculations for various auxiliary gas flow rates above 1.3 L min^{-1}, up to 2.0 L min^{-1}, but the flow pattern remained the same (*cf.* Fig. 11(e)). It can thus be concluded that in order to avoid rotational motion in the carrier gas flow, adjusting the auxiliary gas flow rate helps to some extent, but it is not as effective as changing the carrier gas flow rate.

d.Effect of cooling gas flow rate. Fig. 12 presents the 2D velocity path lines when increasing the cooling gas flow rates from 12 (a) to 14 (b), 16 (c) and 18 (d) L min^{-1}. The carrier gas and auxiliary gas flow rates are kept fixed at 1.0 and 0.4 L min^{-1}, respectively. Note that Fig. 12(a) is the same as Fig. 10(a) and 11(a), for the sake of clarity. It is shown in Fig. 12 that even the highest values of cooling gas flow rates investigated cannot make a significant change in the backward motion of the carrier gas. Indeed, only a tiny improvement is observed in Fig. 12(d). Therefore, in order to avoid the rotational motion of the carrier gas flow, we do not recommend changing the cooling gas flow rate. However, as discussed in Section 3.1.c above, the cooling gas flow rate does affect the rotational motion of the auxiliary gas.

e.Effect of applied power. Finally, we study the effect of applied power on the backward motion of the carrier gas flow. Fig. 13 shows 2D velocity path lines at 1000 (a) and 1200 (b) W. The cooling gas, auxiliary gas and carrier gas flow rates are 12, 0.4 and 1.0 L min^{-1}, respectively. Hence, Fig. 13(a) is again the same as Fig. 10(a), 11(a) and 12(a), for the sake of clarity, except that now the area of external power coupling is added again (see violet contours). Fig. 13(b) illustrates that an increase of 200 watt can improve the rotational behavior of the carrier gas flow to some extent. Indeed, the rotational motion is less pronounced, but it has not completely disappeared. Further increasing the applied power to *e.g.*, 1400 W did not give rise to stable calculation results, at least for the gas flow rates and injector inlet diameter under consideration here. Note that for 1.5 mm injector inlet diameter, no problem occurred when assuming the same gas flow rates and a power as high as 1500 W (*cf.* Fig. 5(d) above).

To work with a higher applied power for an ICP torch fitted with a 2 mm injector diameter, we need to apply higher gas flow rates. This is illustrated in Fig. 14, for 16, 1.2 and 1.2 L min^{-1} of cooling gas, auxiliary gas and carrier gas flow rates, respectively. Note that the cooling gas flow path lines are now added again.

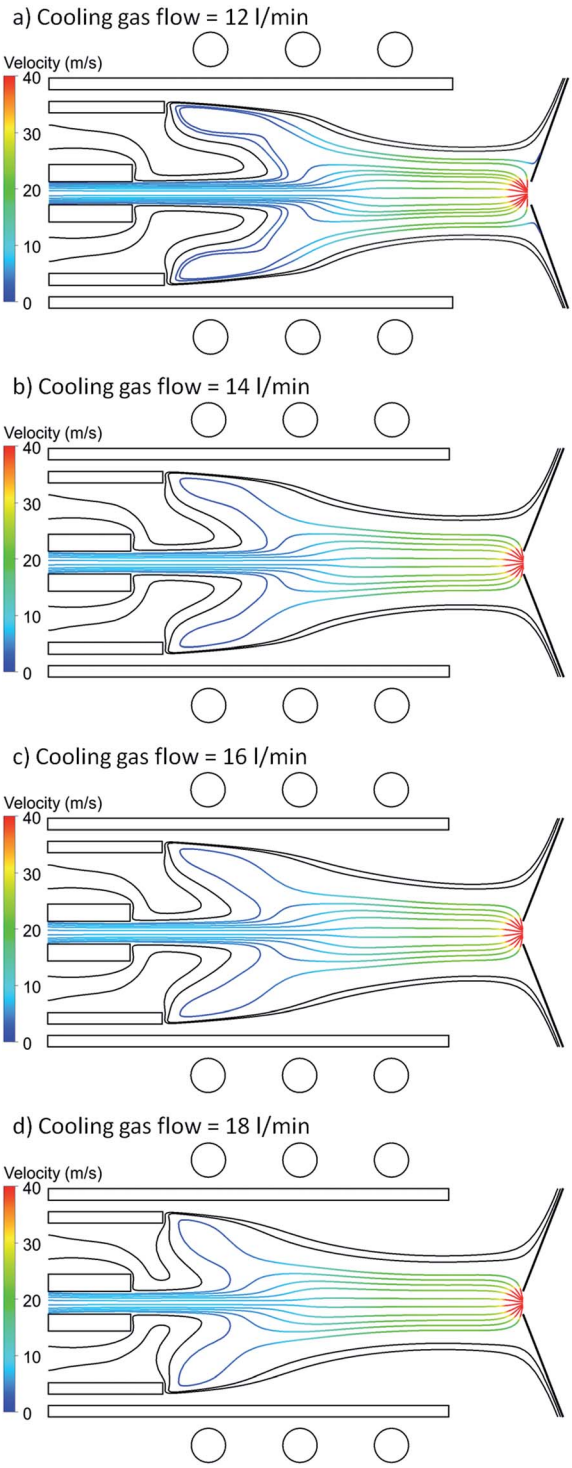

Fig. 12 Effect of cooling gas flow rate: 2D gas flow velocity path lines originating from the carrier gas inlet, colored by velocity in m s^{-1}, and from the auxiliary gas inlet, colored in black. The cooling gas path lines are omitted for the sake of clarity. The cooling gas flow rate is taken as 12 (a), 14 (b), 16 (c) and 18 (d) L min^{-1}. The carrier gas and auxiliary gas flow rates are 1.0 and 0.4 L min^{-1}, respectively. The injector inlet diameter and sampler orifice diameter are 2.0 mm and 1.0 mm, respectively.

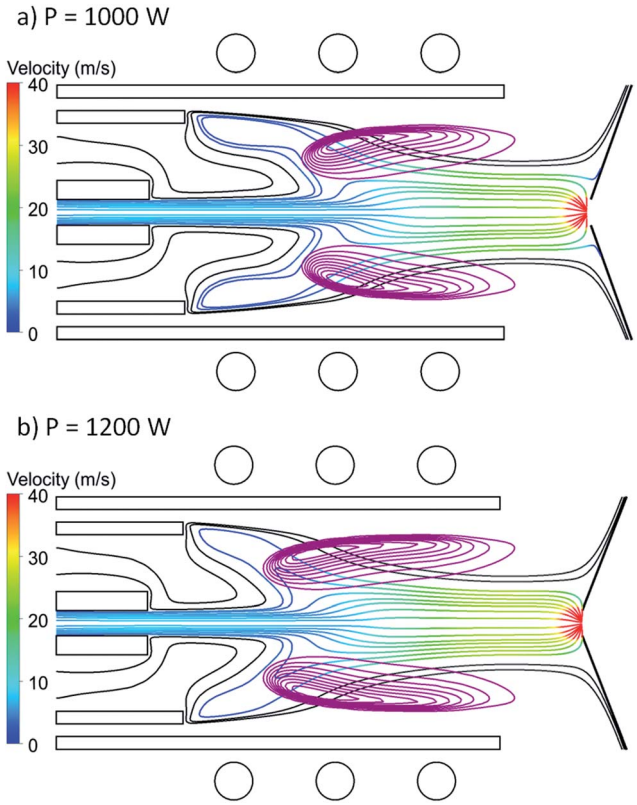

Fig. 13 Effect of power: 2D gas flow velocity path lines originating from the carrier gas inlet, colored by velocity in m s^{-1}, and from the auxiliary gas inlet, colored in black. The cooling gas path lines are omitted for the sake of clarity. The applied power is taken as 1000 (a) and 1200 (b) W. The carrier gas, auxiliary gas and cooling gas flow rates are 1.0, 0.4 and 12 L min^{-1}, respectively. The injector inlet diameter and sampler orifice diameter are 2.0 mm and 1.0 mm, respectively. The violet contours demonstrate the area of external power coupling.

The applied power is 1400 W and the injector inlet diameter is 2 mm. These are typical conditions applied with the Elan 6000 ICP-MS. It is indeed visible that under this condition the carrier gas flow does not move backward at all, and it can entirely

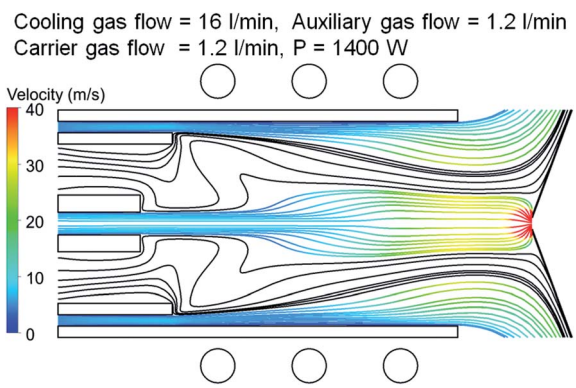

Fig. 14 2D gas flow velocity path lines originating from the carrier gas and cooling gas inlets, colored by velocity in m s^{-1}, and from the auxiliary gas inlet, colored in black. The applied power is taken as 1400 W. The carrier gas, auxiliary gas and cooling gas flow rates are 1.2, 1.2 and 16 L min^{-1}, respectively. The injector inlet diameter and sampler orifice diameter are 2.0 mm and 1.0 mm, respectively.

transfer the introduced sample particles directly to the mass spectrometer. It should be noted that in Fig. 14, the absence of rotational motion of the carrier gas flow is due to an increase of both the applied power and the gas flow rates. We can thus consider Fig. 14 as a result of all parameter effects that we discussed in Section 3.2, and which should be applied to avoid the occurrence of rotational flow behavior in the carrier gas flow path lines.

4. Conclusion

We have computationally investigated the occurrence of rotational motion in the auxiliary and carrier gas flow path lines, in order to obtain better insight into the flow behavior inside the ICP torch and to optimize the transfer from the injector inlets to the sampler orifice. The parameters which play a role to avoid these backward motions were investigated in detail.

Using 1.5 mm injector inlet diameter typically results only in the occurrence of rotational motion in the auxiliary gas flow path lines and not in the carrier gas flow path lines. Our calculations predict that by increasing either the carrier gas, auxiliary gas or cooling gas flow rates, or by raising the external power, we can control and avoid the backward motion of the auxiliary gas. Moreover, using a sampler with a larger orifice diameter also results in a drop in the rotational behavior of the auxiliary gas flow. This can all be explained by a lower shear force between the different gas flows. Our computational results were validated with experiments performed on the Elan 6000 ICP-MS setup, and qualitative agreement was obtained for the effect of applied power. It has to be mentioned that it was not possible to validate the model predictions for the effect of gas flow rates and geometry due to experimental limitations.

Furthermore, our calculation results have demonstrated that by using a larger injector inlet diameter, also the carrier gas flow will exhibit some backward motion inside the torch, which is undesirable for sample transfer to the mass spectrometer. Similar to the auxiliary gas, the backward motion in the carrier gas flow could be reduced by applying higher carrier gas, auxiliary gas or cooling gas flow rates and a higher applied power.

For both the auxiliary and the carrier gas, it was found that a rise in the carrier gas flow rate has a dominant effect on the occurrence of rotational motion, and can thus be used as the most effective parameter to remove the backward flows inside the torch.

It needs to be mentioned that the importance of optimizing the auxiliary and carrier gas path lines will become more clear when we can trace with our model the introduced sample material inside the torch. Indeed, due to different boiling and ionization temperatures of different materials, the position at which the sample or sample cloud may move in the radial direction to the outer region and become further away from the central channel is different.[40,41] Hence, it will be important to know exactly which path line they follow. Moreover, in the future, the optimization of the gas flow motion, which is focused on in the current paper, will have to be combined with signal intensity optimization, which is currently not considered. Indeed, note that an increase in the carrier gas flow rate can lead to low signal intensities because a lower amount of analyte will get ionized due to the high gas flow rate and the low temperature in the plasma. This effect can be studied when the particle tracing is added to the current model. The introduction of sample particles is therefore the next step in our model development. Nevertheless, the study carried out in the present paper has already explained where the samples might get lost and it can predict the parameters which might help to reduce these losses.

Acknowledgements

The authors gratefully acknowledge financial support from the University of Antwerp through the Methusalem Financing. This work was carried out using the Turing HPC infrastructure at the CalcUA core facility of the Universiteit Antwerpen, a division of the Flemish Supercomputer Center VSC, funded by the Hercules Foundation, the Flemish Government (department EWI) and the Universiteit Antwerpen. Furthermore, financial support by the Swiss National Science Foundation (SNSF, project ID 141292) is also gratefully acknowledged.

References

1 R. S. Houk, B. R. LaFreniere, H. B. Lim and V. A. Fassel, Extraction Discharge Source for Enhancing Analyte Line Intensities in Inductively Coupled Plasma Atomic Emission Spectrometry, *Appl. Spectrosc.*, 1987, **41**, 391–395.

2 R. K. Winge, J. S. Crain and R. S. Houk, A High Speed Photographic Study of Plasma Fluctuations and Undissociated Particles in ICP-MS, *J. Anal. At. Spectrom.*, 1991, **6**, 601–604.

3 H. Ma, N. Taylor and P. B. Farnsworth, The effect of the sampling interface on spatial distributions of barium ions and atoms in an inductively coupled plasma ion source, *Spectrochim. Acta, Part B*, 2009, **64**, 384–391.

4 S. A. Lehn, K. A. Warner, M. Huang and G. M. Hieftje, Effect of an inductively coupled plasma mass spectrometry sampler interface on electron temperature, electron number density, gas-kinetic temperature and analyte emission intensity upstream in the plasma, *Spectrochim. Acta, Part B*, 2002, **57**, 1739–1751.

5 D. J. Douglas and J. B. French, Gas dynamics of the inductively coupled plasma mass spectrometry interface, *J. Anal. At. Spectrom.*, 1988, **3**, 743–747.

6 R. L. Spencer, J. Krogel, J. Palmer, A. Payne, A. Sampson, W. Somers and C. N. Woods, Modeling the gas flow upstream and in the sampling nozzle of the inductively coupled plasma mass spectrometer *via* the Direct Simulation Monte Carlo algorithm, *Spectrochim. Acta, Part B*, 2009, **64**, 215–221.

7 R. L. Spencer, N. Taylor and P. B. Farnsworth, Comparison of calculated and experimental flow velocities from the sampling cone of an inductively coupled plasma mass spectrometer, *Spectrochim. Acta, Part B*, 2009, **64**, 921–924.

8 M. Aghaei, H. Lindner and A. Bogaerts, Effect of a mass spectrometer interface on inductively coupled plasma characteristics: a computational study, *J. Anal. At. Spectrom.*, 2012, **27**, 604–610.

9 A. L. Gray and A. R. Date, Inductively coupled plasma source mass spectrometry using continuum flow ion extraction, *Analyst*, 1983, **108**, 1033–1050.

10 J. S. Crain, R. S. Houk and F. G. Smith, Matrix interferences in inductively coupled plasma-mass spectrometry: some effects of skimmer orifice diameter and ion lens voltages, *Spectrochim. Acta, Part B*, 1988, **43**, 1355–1364.

11 M. A. Vaughan and G. Horlick, Effect of sampler and skimmer orifice size on analyte and analyte oxide signals in inductively coupled plasma mass spectrometry, *Spectrochim. Acta, Part B*, 1990, **45**, 1289–1299.

12 H. P. Longerich, B. J. Fryer, D. F. Strong and C. J. Kanttpuly, Effects of operating conditions on the determination of the rare earth elements by inductively coupled plasma-mass spectrometry (ICP-MS), *Spectrochim. Acta, Part B*, 1987, **42**, 75–92.

13 N. Taylor and P. B. Farnsworth, Experimental characterization of the effect of skimmer cone design on shock formation and ion transmission efficiency in the vacuum interface of an inductively coupled plasma mass spectrometer, *Spectrochim. Acta, Part B*, 2012, **69**, 2–8.

14 D. Günther, H. P. Longerich, S. E. Jackson and L. Forsythe, Effect of sampler orifice diameter on dry plasma inductively coupled plasma mass spectrometry (ICP-MS) backgrounds, sensitivities, and limits of detection using laser ablation sample introduction, *Fresenius. J. Anal. Chem.*, 1996, **355**, 771–773.

15 D. Bernardi, V. Colombo, E. Ghedini and A. Mentrelli, Three-dimensional modeling of inductively coupled plasma torches, *Pure Appl. Chem.*, 2005, **77**(2), 359–372.

16 H. Lindner, A. Murtazin, S. Groh, K. Niemax and A. Bogaerts, Simulation and experimental studies on plasma temperature, flow velocity and injector diameter effects for an inductively coupled plasma, *Anal. Chem.*, 2011, **83**, 9260–9266.

17 J. H. Macedone, D. J. Gammon and P. B. Farnsworth, Factors affecting analyte transport through the sampling orifice of an inductively coupled plasma mass spectrometer, *Spectrochim. Acta, Part B*, 2001, **56**, 1687–1695.

18 S. Kaneco, T. Nomizo, T. Tanaka, N. Mizutani and H. Kawaguchi, Optimization of operating conditions in individual airborne particle analysis by inductively coupled plasma mass spectrometry, *Anal. Sci.*, 1995, **11**, 835–840.

19 W. G. Diegor and H. P. Longerich, Parameter interaction in signal optimization of an ICP mass spectrometer, *At. Spectrosc.*, 2000, **21**, 111–117.

20 H. P. Longerich, B. J. Fryer, D. F. Strong and C. J. Kantipuly, Effects of operating conditions on the determination of the rare earth elements by inductively coupled plasma-mass spectrometry (ICP-MS), *Spectrochim. Acta, Part B*, 1987, **42**, 75–92.

21 S. E. Long and R. M. Browner, Optimization in inductively coupled plasma mass spectrometry, *Analyst*, 1986, **111**, 901–906.

22 Q. Xie and R. Kerrich, Optimization of operating conditions for improved precision of zirconium and hafnium isotope ratio measurement by inductively coupled plasma mass spectrometry (ICP-MS), *J. Anal. At. Spectrom.*, 1995, **10**, 99–103.

23 B. T. G. Ting and M. Janghorbani, Optimization of instrumental parameters for the precise measurement of isotope ratios with inductively coupled plasma mass spectrometry, *J. Anal. At. Spectrom.*, 1988, **3**, 325–336.

24 G. Gamez, S. A. Lehn, M. Huang and G. M. Hieftje, Effect of Mass Spectrometric sampling interface on the fundamental parameters of an inductively coupled plasma as a function of its operating conditions. Part I. Applied RF power and vacuum, *Spectrochim. Acta, Part B*, 2007, **62**, 357–369.

25 G. Gamez, S. A. Lehn, M. Huang and G. M. Hieftje, Effect of Mass Spectrometric sampling interface on the fundamental parameters of an inductively coupled plasma as a function of its operating conditions. Part II. Central-gas flow rate and sampling depth, *Spectrochim. Acta, Part B*, 2007, **62**, 370–377.

26 J. H. Macedone, A. A. Mills and P. B. Farnsworth, Optical measurements of ion trajectories through the vacuum interface of an inductively coupled plasma mass spectrometer, *Appl. Spectrosc.*, 2004, **58**, 463–467.

27 G. Horlick, S. H. Tan, M. A. Vaughan and C. A. Rose, The effect of plasma operating parameters on analyte signals in inductively coupled plasma-mass spectrometry, *Spectrochim. Acta, Part B*, 1985, **40**, 1555–1572.

28 M. Aghaei, H. Lindner and A. Bogaerts, Optimization of operating parameters for inductively coupled plasma mass spectrometry: A computational study, *Spectrochim. Acta, Part B*, 2012, **76**, 56–64.

29 M. Aghaei, H. Lindner and A. Bogaerts, Effect of sampling cone position and diameter on the gas flow dynamics in an ICP, *J. Anal. At. Spectrom.*, 2013, **28**(9), 1485–1492.

30 R. M. Belchamber and G. Horlick, Noise-power spectra of optical and acoustic emission signals from an inductively coupled plasma, *Spectrochim. Acta, Part B*, 1982, **37**, 17–27.

31 G. K. Batchelor, *Introduction to Fluid Dynamics*, Cambridge University Press, Cambridge, 1967.

32 L. D. Landau and E. M. Lifshitz, *Fluid Mechanics*, Pergamon Press, Oxford, 2nd edn, 1987.

33 L. Flamigni, J. Koch and D. Günther, Experimental and theoretical investigations about the vaporization of laser-produced aerosols and individual particles inside inductively coupled plasmas – Implications for the extraction efficiency of ions prior to mass spectrometry, *Spectrochim. Acta, Part B*, 2012, **76**, 70–76.

34 ANSYS FLUENT 12.0/12.1 Documentation, 2009.

35 H. Lindner and A. Bogaerts, Multi-element model for the simulation of inductively coupled plasmas: Effects of helium addition to the central gas stream, *Spectrochim. Acta, Part B*, 2011, **66**, 421–431.

36 iStar DH734, Andor, Belfast, Northern Ireland.

37 J. Schindelin, I. Arganda-Carreras, E. Frise, V. Kaynig, M. Longair, T. Pietzsch, S. Preibisch, C. Rueden, S. Saalfeld, B. Schmid, J. Y. Tinevez, D. J. White, V. Hartenstein, K. Eliceiri, P. Tomancak and A. Cardona, Fiji: an open-source platform for biological-image analysis, *Nat. Methods*, 2012, **9**, 676–682.
38 C. A. Schneider, W. S. Rasband and K. W. Eliceiri, NIH Image to ImageJ: 25 years of image analysis, *Nat. Methods*, 2012, **9**, 671–675.
39 http://www.perkinelmer.com/Catalog/Product/ID/N8125029.
40 D. C. Perdian, S. J. Bajic, D. P. Baldwin and R. S. Houk, Time-resolved Studies of Particle Effects in Laser Ablation ICP-MS Part I. Investigation of Nanosecond and Femtosecond Pulse Width Lasers and Devices for Particle Size Selection, *J. Anal. At. Spectrom.*, 2008, **23**, 325–335.
41 K. Niemax, Considerations about the detection efficiency in inductively coupled plasma mass spectrometry, *Spectrochim. Acta, Part B*, 2012, **76**, 65–69.